Submitted to *Journal of Alloys and Compounds*, September 2011; Revised December 2011

In-situ formation of ZrB_2-ZrO_2 ultra-high-temperature ceramic composites from high-energy ball-milled ZrB_2 powders

Victor Zamora [a], Angel L. Ortiz [a,*], Fernando Guiberteau [a], Mats Nygren [b]

[a] Departamento de Ingeniería Mecánica, Energética y de los Materiales,
Universidad de Extremadura, 06006 Badajoz, Spain

[b] Department of Materials and Environmental Chemistry, University of Stockholm,
10691 Stockholm, Sweden

Abstract

The *in-situ* formation is reported of a fine-grained ZrB_2 ultra-high-temperature ceramic (UHTC) containing evenly distributed ZrO_2 of uniform size located at triple joints and grain boundaries of the ZrB_2 grains, discovered during the spark-plasma sintering of ZrB_2 powders subjected to high-energy ball-milling in air. It is found that this type of microstructure forms because the oxide film of ZrO_2, developed on the surface of the ZrB_2 particles during the high-energy ball-milling in air, creeps towards the ZrB_2 multigrain joints under the application of pressure during sintering, and then crystallizes there during the fast cooling down to room-temperature. Together with the mechanism by which these dense ZrB_2–ZrO_2 UHTC composites form, it is also shown that they are simultaneously harder and much tougher than their ZrB_2 monolith counterpart.

Keywords: ZrB_2; Ultra-high-temperature ceramics; Spark-plasma sintering.

* Corresponding author:
Angel L. Ortiz
Phone: +34 924289600 Ext: 86726
Fax: +34 924289601
E-mail: **alortiz@materiales.unex.es**

1. Introduction

Zirconium diboride (ZrB_2) is an ultra-high-temperature ceramic (UHTC) that generates great interest in the aerospace sector, in particular for the protection of vehicle aerosurfaces exposed to high-flow environments of hot oxidizing gases, as is the case in hypersonic flights and atmospheric re-entry [1-2]. However, ZrB_2 alone is very brittle and does not have sufficient toughness, strength, and thermal shock resistance to be used successfully for such aerospace applications [1-2]. Reducing this inherent brittleness has thus become a critical issue to ensure the mechanical integrity of ZrB_2 UHTCs when they are in service. The strategy adopted to achieve this goal consists of engineering the microstructure of the ZrB_2 UHTCs, normally by the addition of second phases [1-26] and sometimes also by the fabrication of laminated-type architectures with compressive residual stresses [27-29] or of complex cell-type architectures [30]. SiC is the typical second phase particle in ZrB_2 [1-3], and its introduction improves the toughness because of the crack defection and crack-wake bridging in the weak ZrB_2–SiC interfaces. The addition of SiC also enhances the strength of ZrB_2 because SiC inhibits grain growth thus reducing the dominant initial flaw size. Other ceramic second phases such as $MoSi_2$, ZrC, HfN, and TiN [1,2,4], or combinations of various second phases [1,2,4-7], that improve densification may also inhibit grain growth improving the strength and toughness of the material. However, ductile Nb and Mo metal particles have also been added to ZrB_2 [8,9], which has been observed to favour crack deflection and branching as well as to promote stress relaxation near the crack trip [8]. The incorporation of high aspect ratio reinforcements, such as carbon fibres [10,11] and nanotubes [12], graphite flakes [13-16], and SiC whiskers [17-20], fibres [17,18], or platelets [21] further reduces the brittleness of the ZrB_2-based composites, which is attributed to the combination of debonding, pull-out and bridging of these reinforcements as well as enhanced crack deflection and crack pinning. Finally, another interesting strategy lies in dispersing within the ZrB_2 matrix a second phase with phase-transformation capability, such as ZrO_2 [22-26]. Thus, it has been demonstrated that the ZrB_2–ZrO_2 composites exhibit *R*-curve behaviour while pure ZrB_2 ceramics do not [22-24], resulting from crack bridging and the stress-induced martensitic transformation in ZrO_2. So far, the ZrB_2–ZrO_2 particulate composites have been fabricated from mixtures of ZrB_2 and ZrO_2 powders (the preparation of which involves comminution, wet homogenization, and slurry drying) that are densified by hot-pressing resulting in a duplex ceramic microstructure.

In this context, here a simpler route is reported that results in the *in-situ* formation of fine-grained ZrB_2 UHTCs containing evenly distributed ZrO_2 of uniform size located at triple joints and grain boundaries of the ZrB_2 grains. The formation of these ZrB_2–ZrO_2 composites was discovered during the spark-plasma sintering (SPS) of ZrB_2 powders refined by high-energy ball-milling in air. The technique of SPS is similar to the more classical hot-pressing in that both apply uniaxial load, although SPS has the advantage that the pulsed electrical current heats the die (and the compact if the powder is electrically conductive) directly, and the rapid sintering cycles enable a better control of the final microstructure and therefore of the properties of the resulting material [31]. The objective of the present study is to describe the *in-situ* formation mechanism of these ZrB_2–ZrO_2 UHTC composites, and to propose how these and other ZrB_2–oxide UHTC composites could be processed more controllably in the future.

2. Experimental procedures

The ZrB_2 starting powder was obtained from a commercial source (Grade B, H.C. Starck, Goslar, Germany). This ZrB_2 powder has a purity of 96-97% according to the manufacturer indication, an oxygen content of 1.5 wt% based on the measurement by fusion in inert gas, and consists of micrometre particles with an average size of 2–3 μm. To reduce its particle size, the as-received ZrB_2 powder was subjected to high-energy ball-milling in air for 180 min in a shaker mill (Spex D8000, Spex CertiPrep, USA) operated at about 1060 back-and-forth cycles per minute. The milling was carried out in a cylindrical hardened-steel container with WC balls (6.7mm in diameter; Union Process Inc., USA) under a ball-to-powder weight ratio of 4:1[a]. This milling condition has been proved to be effective in refining ZrB_2 to nano-crystallites with ~10 nm average size [32-34], as is also shown here in the transmission electron microscopy images of Fig. 1. The ball-milled ZrB_2 powder, which contains 4.5 wt% oxygen according to the measurement by fusion in inert gas and 2.5 wt% WC (taken from milling media) according to the X-ray diffraction (XRD) analysis [34], was then spark-plasma sintered (Dr. Sinter SPS-2050, Sumitomo Coal Mining Co., Japan) at 1900 °C with 75 MPa for 3 min in a dynamic vacuum (i.e., ~6 Pa), within a graphite die lined with graphite foil and surrounded by a 1 cm thick graphite blanket to minimize the heat loss.

[a] To minimize the powder contamination during high-energy ball-milling, a first milling cycle was carried out with the objective of depositing a thin film of ZrB_2 on the surface of the container and of the balls, and the resulting powder was thrown away. Then, the milling cycle was repeated using the same container and balls, using the resulting powder for this study.

The heating ramp was set at 200 °C·min^{-1} with 50 MPa up to 1200 °C, and at 100 °C·min^{-1} with 75 MPa from 1200 to 1900 °C. The application of the 50 MPa pressure was done at room-temperature, and at 1200 °C the pressure was increased rapidly up to 75 MPa at a rate of 2 MPa·s^{-1}. After the completion of the sintering cycle, the load was released and the electrical power was shut off to allow rapid cooling to room temperature (i.e., in 1–2 min).

The density of the resulting ceramic was measured using the Archimedes principle with distilled water as the immersion medium. The microstructural characterization was performed by scanning electron microscopy (SEM; S-3600N, Hitachi, Japan), energy dispersive X-ray spectroscopy (EDXS; XFLASH Detector 3001, Röntec GmbH, Germany), and XRD (D8 Advance, Bruker AXS, Germany), using in all cases routine procedures applicable to ceramics. The hardness (H) and toughness (K_{IC}) were evaluated by Vickers-indentation tests (98 N load, P), using standard formulae for the calculations (i.e., $H=P/2a^2$ and $K_{IC}= 0.016(E/H)^{0.5}Pc^{-1.5}$, where $2a$ and $2c$ are the diagonals and radial-crack diameters (surface traces) of the indents, respectively, and E is the Young modulus which is 517 GPa for this ZrB_2-ZrO_2 composite) [35].

A reference material was also prepared by spark-plasma sintering the as-received ZrB_2 powder under identical conditions as the ball-milled ZrB_2 powder, and its microstructure and mechanical properties were determined as well to be used as a comparison baseline. The Young modulus of this ZrB_2 monolith used for calculation of its toughness is 540 GPa.

3. Results and discussion

Fig. 2A shows a representative SEM micrograph of the UHTC fabricated from the 180-min ball-milled ZrB_2 powder. The average ZrB_2 grain size is ~5 μm, which is relatively small compared to the ~15 μm grain size of the reference ZrB_2 monolith prepared from the as-received ZrB_2 powder (Fig. 2B). The reference monolith contains pores located at triple joints, grain edges, and especially within the grains, as seen more clearly in the optical micrograph of Fig. 3. The SEM micrograph of Fig. 2A also displays the presence of smaller particles (i.e., ~1 μm) that exhibit a slight compositional contrast. The EDXS analysis of these small particles shown in Fig. 4A indicates that they are ZrO_2, and the XRD analysis of the compact shown in Fig. 4B that this ZrO_2 crystallized in its monoclinic and tetragonal variants with the total amount of ZrO_2 representing ~8 wt%. Thus, the combination of the SEM, EDXS, and XRD analyses reveals that the UHTC fabricated from the ball-milled ZrB_2 powder is indeed a ZrB_2–ZrO_2 composite.

The hardness and toughness measured by Vickers testing were 17.6(±0.2) GPa and 3.0(±0.1) MPa·$m^{0.5}$ for the ZrB_2–ZrO_2 composite, and 16.2(±0.2) GPa and 1.9(±0.1) MPa·$m^{0.5}$ for the reference ZrB_2 monolith. The increased toughness of the ZrB_2–ZrO_2 composite compared to the reference ZrB_2 monolith, which has a grain size more than twice as large, highlights the fundamental role of ZrO_2 in enhancing the ZrB_2 toughness via crack bridging and its transformation toughening in accordance with previous observations [22-24]. Furthermore, despite ZrO_2 being softer than ZrB_2, the ZrB_2–ZrO_2 composite is harder than the reference ZrB_2 monolith, in part because the former is fully dense whereas the latter is only ~96% dense (see Figs. 2B and 3).

The remarkable characteristic of the ZrB_2–ZrO_2 UHTC composite prepared in this study is its microstructure. Previously, ZrB_2–ZrO_2 composites have been fabricated from the typical mechanical mixture of ZrB_2 and ZrO_2 powders [22-24]. As such, they have the classical duplex microstructure, with micrometre-sized ZrO_2 grains dispersed between coarser ZrB_2 grains. In the present case, however, the ZrB_2–ZrO_2 composite has a different microstructure, with submicrometre ZrO_2 particles located in the grain boundaries and multigrain junctions of fine ZrB_2 grains. Importantly, the fabrication route of this ZrB_2–ZrO_2 composite does not require the explicit incorporation of ZrO_2 particles, since they form *in-situ* during the SPS of the ZrB_2 powder previously subjected to high-energy ball-milling in air, which notably simplifies the processing route. Thus, the ZrO_2 phase arises from the surface oxidation itself of ZrB_2 that occurs during the high-energy ball-milling in air [36], which, as will be demonstrated below, is actually the key to obtaining that particular microstructure. In addition to ZrO_2, B_2O_3 is also formed during this oxidation [36] but is not retained during the SPS at high temperatures, as will be discussed below.

To elucidate the formation mechanism of this ZrB_2–ZrO_2 UHTC composite, a series of model experiments was conducted in which the electrical power of the SPS furnace was shut off at lower temperatures. Owing to the rapid cooling to room temperature of the SPS furnace, the micrographs taken from these samples can be considered “frozen” pictures of the microstructure of the ZrB_2–ZrO_2 composite during the heating ramp, thus providing a good method for monitoring its microstructural development. Fig. 5A is a representative SEM micrograph of the sample obtained at 1700 °C, showing many grain boundaries without apparent evidence of other phases. However, the extensive SEM observations revealed the existence of another two types of grain boundaries/faces. One of these can be observed in Fig. 5A, but is shown in more details in the

SEM micrograph of Fig. 5B. It consists of a phase with viscous appearance located at grain boundaries and multigrain joints, which was identified by EDXS as being ZrO_2. The other type of grain-boundary structure is shown in the SEM micrograph of Fig. 5C. It can be seen that some grain faces exhibit what appears to be a dendritic-like structure. This type of structure was rarely found in the sample obtained at 1700 °C, and was not observed during the SEM examination of the ZrB_2–ZrO_2 composite sintered at 1900 °C, indicating that it is transient. The probable explanation is that this dendritic-like structure originated due to the fast condensation (fast cooling rates greater than 600 °C·min^{-1} are achieved when the electrical power in the SPS is shut off) of the gaseous B_2O_3 formed during the heating ramp. Sublimation of B_2O_3 in the temperature range 1400–1650 °C is a well-know phenomenon in ZrB_2 UHTCs, and is indeed the method used to remove the B_2O_3 impurities present on the surface of the ZrB_2 particles with a view to facilitating sintering [37,38]. Since according to the densification curve shown in Fig. 6 the relative density in the temperature range 1400–1650 °C varies in the interval ~65–88%, and the SPS test was done in dynamic vacuum (~6 Pa), most of the B_2O_3 gas generated was eliminated during the heating ramp, whereas the still-enclosed B_2O_3 gas at 1700 °C condensed dendritically when exposed to the ultra-fast cooling to room temperature. However, the B_2O_3 gas is completely eliminated at higher sintering temperatures, as proved by the absence of the dendritic-like structure in the ZrB_2–ZrO_2 UHTC composite sintered at 1900 °C, and the observation that the vacuum level temporary dropped from ~6 to 8 Pa and then recovered its level of ~6 Pa.

With these SEM/EDXS observations, it is very reasonable to think that the formation of the ZrB_2–ZrO_2 UHTC composites occurs as follows. Initially during the high-energy ball-milling in air, the ZrB_2 particles oxidize superficially, developing an amorphous oxide film of ZrO_2 and B_2O_3 [36]. Subsequently, during the heating ramp under dynamic vacuum atmosphere, the B_2O_3 impurities are removed by sublimation, while the ZrO_2 film creeps due to the applied pressure (75 MPa in the present case). Note that the creep literature has shown sufficient experimental evidence that ZrO_2, and in particular the monoclinic and tetragonal phases, can creep appreciably below 1400 °C at 50 MPa [39-43], which are temperatures and pressures lower than used here. At the intermediate stage of sintering when, according to Coble's model [44], an interconnected cylindrical pore structure exists along the grain edges as schematized by the idealized geometry of Fig. 7A, the viscous ZrO_2 is then squeezed out from grain faces under compression and accumulates within the pore structure network. Later during the heating ramp already in the final

stage of sintering when, again according to Coble's model [44], the open pore structure collapses and evolves towards discrete spherical pores located at grain corners as sketched in Fig. 7B, the viscous ZrO_2 flows to the multigrain joints. Upon fast cooling to room temperature, the viscous ZrO_2 entrapped at multigrain joints crystallizes there in part as monoclinic ZrO_2 because this is the stable polymorph in the absence of doping. However, the high-temperature tetragonal polymorph is also present at room temperature, possibly stabilized by some 3+ solute ions (i.e., B^{3+}) as has been observed before for Al^{3+} [45], or simply retained by the ultra-fast cooling in the SPS.

The proposed mechanism is consistent with the densification curve measured experimentally. As shown in Fig. 6, there is a clear increase in densification between ~1450 °C and 1600 °C, as would be expected from the formation and flow of a viscous phase. However, there is no full densification by pore filling due to the insufficient volume fraction of viscous ZrO_2 formed (~8 wt% equivalent to ~8 vol% because the densities of ZrB_2 and ZrO_2 are very similar). Furthermore, the subsequent densification does not proceed via liquid-phase sintering, but by solid-state sintering, because ZrO_2 does not form a continuous liquid matrix that embeds the ZrB_2 grains.

With the mechanism of microstructural development proposed above, the formation of these ZrB_2–ZrO_2 UHTC composites might not be exclusive of the ZrB_2 powder subjected to high-energy ball-milling for 180 min in air, but may also occur for any ZrB_2 powder as long as it oxidizes sufficiently during ball-milling. This assumption has been explored here using two ZrB_2 powders subjected to high-energy ball-milling in air for 10 and 30 min, respectively, and then spark-plasma sintered under the same conditions as the powder with 180 min of high-energy ball-milling. The average crystallites size in these two ZrB_2 powders is 70 and 25 nm [34], respectively, and their oxygen content is 3.4 and 4.1 wt%, respectively. These results and the previous ones for the powder with 180 min of ball milling indicate that the oxygen content increases and the crystallite size decreases with increasing high-energy ball-milling time. As can be observed in Fig. 8, the SEM micrographs confirm the formation of ZrB_2–ZrO_2 UHTC composites in both cases, with different ZrB_2 grain sizes (~10 and 7 μm, respectively) and ZrO_2 contents (~3 and 7 wt%, respectively). It can thus be inferred from the microstructural observations (Figs. 2A, 8A, and 8B) that the longer the high-energy ball-milling time of the ZrB_2 powder, the smaller the ZrB_2 grain size and the higher the ZrO_2 content in the ZrB_2–ZrO_2 UHTC composites. Consequently, it is reasonable to think that in principle it would be possible to control the microstructure of these

ZrB_2–ZrO_2 UHTC composites to some extent by the judicious selection of the high-energy ball-milling conditions, in particular of the time and atmosphere (oxygen partial pressure, stationary or dynamic, etc.), together with the optimization of the sintering protocol. Note that the spontaneous passivation of ZrB_2 in contact with air at room-temperature after high-energy ball-milling is not a concern due to the controlled oxidation of ZrB_2 during milling.

In view of the above results, it is worthwhile to examine briefly the reasons why this type of ZrB_2–ZrO_2 UHTC composite has not been observed before. This is most likely due to a combination of two factors. Firstly, the commercially-available ZrB_2 powders are typically refined by wet attrition milling under inert atmosphere, and thus the resulting powders have lower oxygen contents and, in addition, are submicrometric. Secondly, the attrition-milled powders are commonly densified either by pressureless sintering or hot-pressing with the help of additives (such as C, B_4C, and WC) that act as reductants removing the surface oxides, because these oxides favour coarsening over densification [1]. In the present study, by contrast, the densification by SPS of the ZrB_2 nano-powders prepared by high-energy ball-milling in air was done without the explicit incorporation of reductants. Note however that the high-energy ball-milling might introduce WC, although in an amount insufficient to reduce all the ZrO_2 formed during the milling in air, and in addition, the reduction reaction is not favoured by the SPS conditions used (rapid sintering for only 3 min at 1900 °C).

Having discovered a route to fabricate ZrB_2–ZrO_2 UHTC composites with original microstructures, the next step will be to reproduce this process more controllably and to extend it to other ZrB_2-oxide composites. It is proposed that this could be done by impregnating the ZrB_2 powder particles obtained by high-energy ball-milling under controlled conditions with oxide solutions prepared by the sol-gel method, and then spark-plasma sintering or hot-pressing these oxide-coated ZrB_2 powders, since the use of pressure is vital for the oxide phase to creep. If successful, this would appear to be a versatile method for processing a wide variety of ZrB_2 UHTC composites containing the desired proportion of evenly distributed oxide particles of uniform size, customized chemistry, and defined crystal structure located at grain boundaries and multigrain joints, and consequently could be used to provide the ZrB_2 UHTCs with tailored properties. This, however, remains to be explored experimentally.

4. Conclusions

The mechanism has been presented of *in-situ* formation of dense ZrB_2–ZrO_2 UHTC composites, discovered during the spark-plasma sintering of ZrB_2 powders subjected to high-energy ball-milling in air. These composites exhibit original microstructures consisting of submicrometre ZrO_2 particles located in the grain boundaries and multigrain junctions of fine ZrB_2 grains, and form because the oxide film of ZrO_2 developed on the surface of the ZrB_2 particles during the high-energy ball-milling creeps towards the ZrB_2 multigrain joints under the application of pressure during sintering. Besides identifying the formation mechanism, it has also been shown that these engineered ZrB_2–ZrO_2 UHTC composites are denser and have finer grains than the ZrB_2 monolithic fabricated under the same conditions of spark-plasma sintering, and in addition, they are also simultaneously harder and much tougher.

Acknowledgements

This work was supported by the Ministerio de Ciencia y Tecnología (Government of Spain) and FEDER funds under Grant N° MAT 2007-61609.

References

[1] W.G. Fahrenholtz, G.E. Hilmas, I.G. Talmy, J.A. Zaykoski, J. Am. Ceram. Soc. 90 (2007) 1347–1364.

[2] S.Q. Guo, J. Eur. Ceram. Soc. 29 (2009) 995–1011.

[3] S.C. Zhang, G.E. Hilmas, W.G. Fahrenholtz, J. Eur. Ceram. Soc. 31 (2011) 893–901.

[4] Y. Wang, J. Liang, W. Han, X. Zhang, J. Alloys Compd. 475 (2009) 762–765.

[5] X. Zhang, X. Li, J. Han, W. Han, C. Hong, J. Alloys Compd. 465 (2008) 506–511.

[6] J. Liang, Y. Wang, G. Fang, J. Han, J. Alloys Compd. 493 (2010) 695–698.

[7] W.M. Guo, Z.G. Yang, G.J. Zhang, Int. J. Refract. Met. 29 (2011) 452–455.

[8] X. Sun, W. Han, P. Hu, Z. Wang, X. Zhang, Int. J. Refrac. Met. Hard Mater. 28 (2010) 472–474.

[9] H.L. Wang, D.L. Chen, C.A. Wang, R. Zhang, D.N. Fang, Int. J. Refrac. Met. Hard Mater. 27 (2009) 1024–1026.

[10] F. Yang, X. Zhang, J. Han, S. Du, Mater. Des. 29 (2008) 1817–1820.

[11] F. Yang, X. Zhang, J. Han, S. Du, J. Alloys Compd. 472 (2009) 395–399.

[12] W.B. Tian, Y.M. Kan, G.J. Zhang, P.L. Wang, Mater. Sci. Eng. A 487 (2008) 568–573.

[13] S.B. Zhou, Z. Wang, W. Zhang, J. Alloys Compd. 485 (2009) 181–185.

[14] W. Zhi, Q. Qiang, W. Zhanjun, S. Guodong, J. Alloys Compd. 509 (2011) 6871–6875.

[15] Z. Wang, S. Wang, X. Zhang, P. Hu, W. Han, C. Hong, J. Alloys Compd. 484 (2009) 390–394.

[16] P. Zhou, P. Hu, X. Zhang, W. Han, Scripta Mater. 64 (2011) 276–279.

[17] L. Silvestroni, D. Sciti, C. Melandri, S. Guicciardi, J. Eur. Ceram. Soc. 30 (2010) 2155–2164.

[18] S. Guicciardi, L. Silvestroni, M. Nygren, D. Sciti, J. Am. Ceram. Soc. 93 (2010) 2384–2391.

[19] P. Zhang, P. Hu, X. Zhang, J. Han, S. Meng, J. Alloys Compd. 472 (2009) 358–362.

[20] X. Zhang, L. Xu, S. Du, C. Liu, J. Han, W. Han, J. Alloys Compd. 466 (2008) 241–245.

[21] M. Wang, C.A. Wang, X. Zhang, Mater. Des. 34 (2012) 293–297.

[22] W. Li, X. Zhang, C. Hong, W. Han, J. Han, J. Eur. Ceram. Soc. 29 (2009) 779–786.

[23] W. Li, Y. Zhang, X. Zhang, C. Hong, W. Han, J. Alloys Compd. 478 (2009) 386–391.

[24 T. Zhu, W. Li, X. Zhang, P. Hu, C. Hong, L. Weng, Mater. Sci. Eng. A 516 (2009) 297–301.

[25] L. Jia, Z. Xinghong, W. Zhib, H. Wenboa, J. Hua, Mater. Des. 34 (2012) 853–856.

[26] L. Jia, Z. Xinghong, W. Zhi, H. Wenbo, Scripta Mater. 64 (2011) 872–875.

[27] X. Zhang, P. Zhou, P. Hu, W. Han, J. Eur. Ceram. Soc. 31 (2011) 2415–2423.

[28] C. Wei, X. Zhanga, P. Hua, W. Hana, G. Tianb, Scripta Mater. 65 (2011) 791–794.

[29] Z. Lü, D. Jiang, J. Zhang, Q. Lin, Z. Huang, J. Eur. Ceram. Soc., in press (2011), doi:10.1016/j.jeurceramsoc.2011.04.020.

[30] J.W. Zimmermann, G.E. Hilmas, W.G. Fahrenholtz, J. Am. Ceram. Soc. 92 (2009) 161–166.

[31] Z.A. Munir, D.V. Quach, M. Ohyanagi, J. Am. Ceram. Soc. 94 (2011) 1–19.

[32] C.A. Galán, A.L. Ortiz, F. Guiberteau, L.L. Shaw, J. Am. Ceram. Soc. 92 (2009) 3114–3117.

[33] C.A. Galán, A.L. Ortiz, F. Guiberteau, L.L. Shaw, J. Am. Ceram. Soc. 93 (2010) 3072–3075.

[34] V. Zamora, A.L. Ortiz, F. Guiberteau, L.L. Shaw, M. Nygren, J. Eur. Ceram. Soc. 31 (2011) 2407–2414.

[35] B.R. Lawn, Fracture of Brittle Solids, 2nd edition, Cambridge University Press, Cambridge, U.K., 1993.

[36] A.L. Ortiz, V. Zamora, F. Rodríguez-Rojas, Ceram. Int., in press (2011), doi:10.1016/j.ceramint.2011.11.058.

[37] S.C. Zhang, G.E. Hilmas, W.G. Fahrenholtz, J. Am. Ceram. Soc. 89 (2006) 1544–1550.

[38] W.G. Fahrenholtz, G.E. Hilmas, S.C. Zhang, S. Zhu, J. Am. Ceram. Soc. 91 (2008) 1398–1404.

[39] E. Zapata-Solvas, D. Gómez-García, C. García-Gañán, A. Domínguez-Rodríguez, J. Eur. Ceram. Soc. 27 (2007) 3325–3329.

[40] M. Jiménez-Melendo, A. Domínguez-Rodríguez, A. Bravo-León, J. Am. Ceram. Soc. 81 (1998) 2761–2776.

[41] C. Lorenzo-Martín, D. Gómez-García, A. Gallardo-López, A. Domínguez-Rodríguez, R. Chaim, Scripta Mater. 50 (2004) 1151–1155.

[42] M. Jiménez-Melendo, A. Domínguez-Rodríguez, Acta Mater. 48 (2000) 3201–3210.

[43] M.J. Roddy, W.R. Cannon, G. Skandan, H. Hahn, J. Eur. Ceram. Soc. 22 (2002) 2657–2662.

[44] R.L. Coble, J. Appl. Phys. 32 (1961) 787–792.

[45] A.L. Vasiliev, N.P. Padture, X. Ma, Acta Mater. 54 (2006) 4913–4920.

Figure captions

Figure 1. (A) TEM bright-field image and (B) TEM dark-field image of the ZrB_2 powder with 180 min of high-energy ball-milling in air, showing both primary nano-particles with ~10 nm size.

Figure 2. SEM micrographs (taken with backscattered electrons from the fracture surface) of the ZrB_2 UHTCs processed from (A) the powder with 180 min of high-energy ball-milling in air, and (B) the as-received powder.

Figure 3. Optical micrograph (taken from the etched, polished surface) of the ZrB_2 UHTC processed from the as-received powder. Etching was carried out by polishing with a colloidal silica suspension.

Figure 4. (A) Energy-dispersive X-ray spectra taken in spot mode on the small particles in the BSE-SEM micrograph of Fig. 1A. (B) X-ray diffraction pattern of the ZrB_2 UHTC processed from the 180-min ball-milled powder; the phase identification is included, and the logarithmic Y-scale is to facilitate the appreciation of the monoclinic (m) and tetragonal (t) ZrO_2 peaks.

Figure 5. SEM micrographs (taken with secondary electrons from the fracture surface) of the different types of grain boundaries/faces observed during the heating ramp at 1700 °C for the powder with 180 min of high-energy ball-milling in air, showing (A) many ZrB_2-ZrB_2 contacts without any presence of other phases, (B) a viscous phase at grain boundaries and multigrain joints, and (C) a dendritic-like structure on some grain faces.

Figure 6. SPS-densification curve as a function of temperature for the ZrB_2 powder with 180 min of high-energy ball-milling in air.

Figure 7. Schematic representation of three grains and the pore structure during the (A) intermediate and (B) final stages of sintering, according to Coble's model. The actual microstructure consists of many of these units packed to fill the space.

Figure 8. SEM micrographs (taken with backscattered electrons from the fracture surface) of the ZrB_2 UHTCs processed from the powders subjected to high-energy ball-milling in air for (A) 10 min, and (B) 30 min.

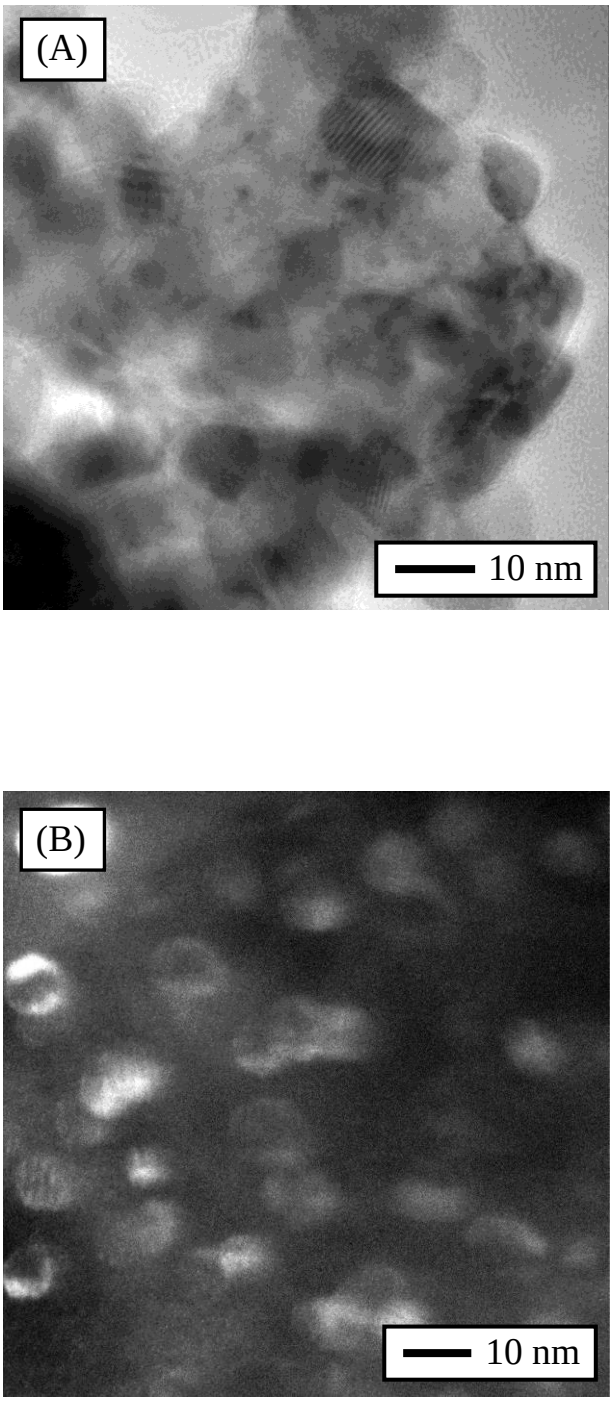

V. Zamora *et al.*
Figure 1

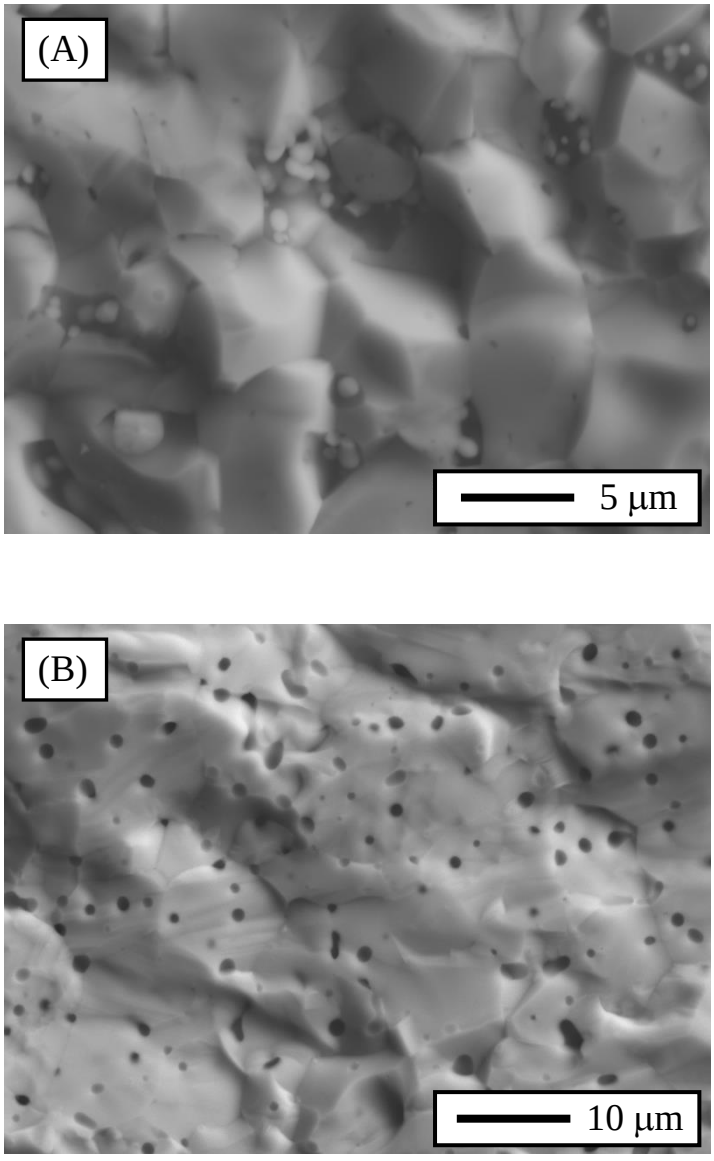

V. Zamora *et al.*
Figure 2

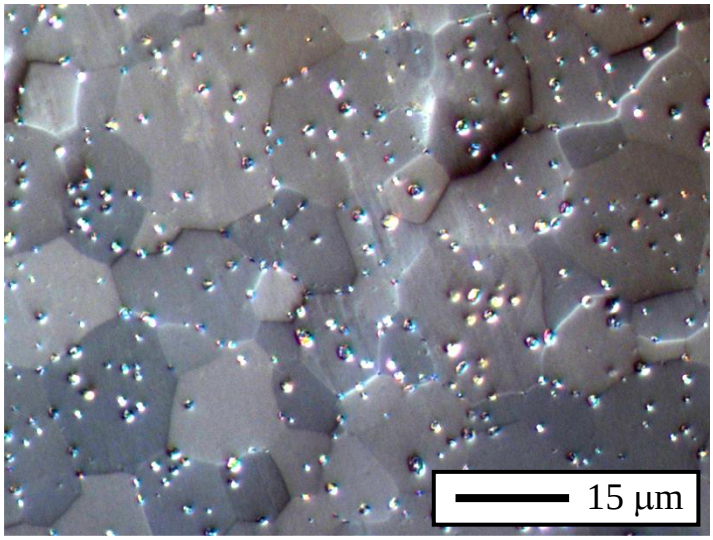

V. Zamora *et al.*
Figure 3

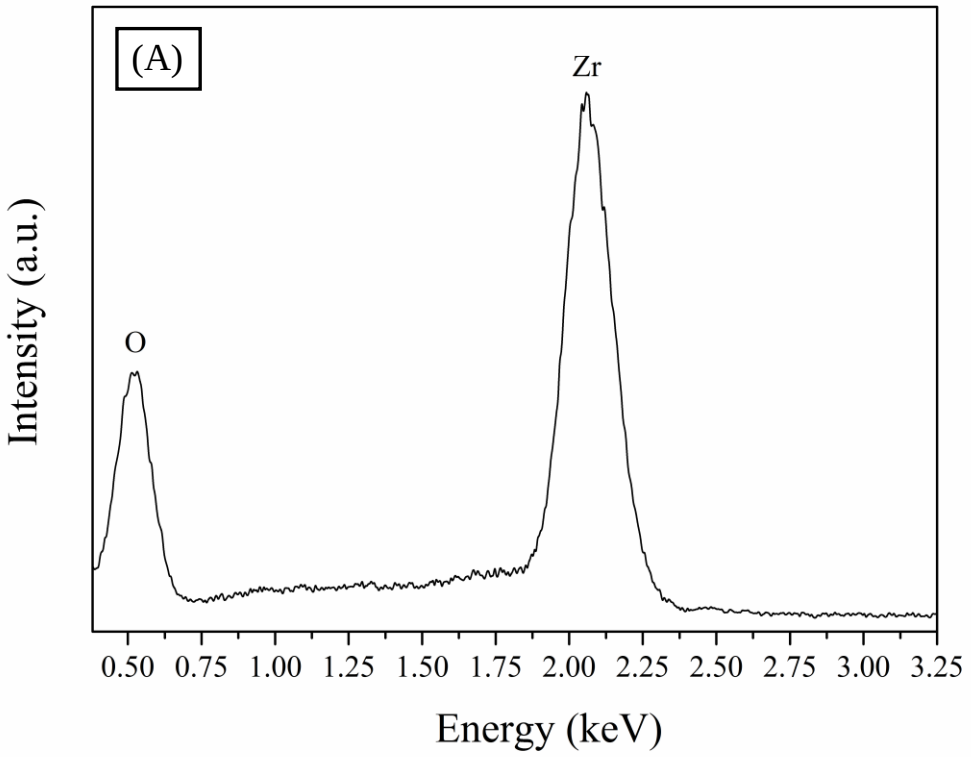

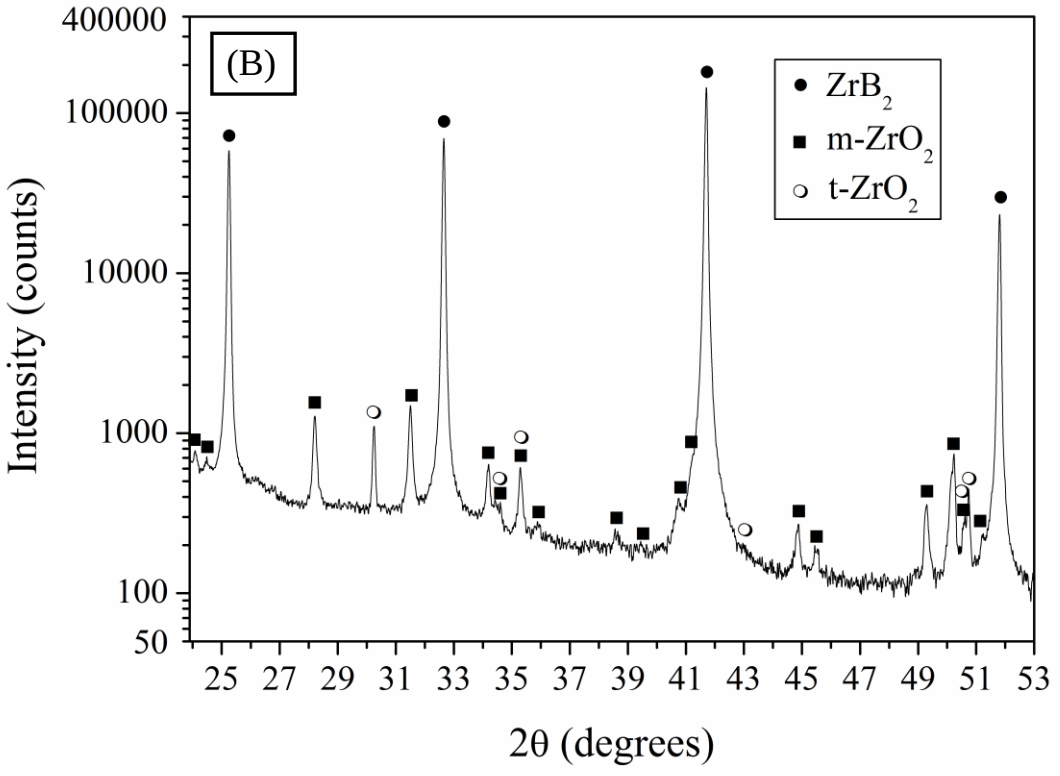

V. Zamora *et al.*
Figure 4

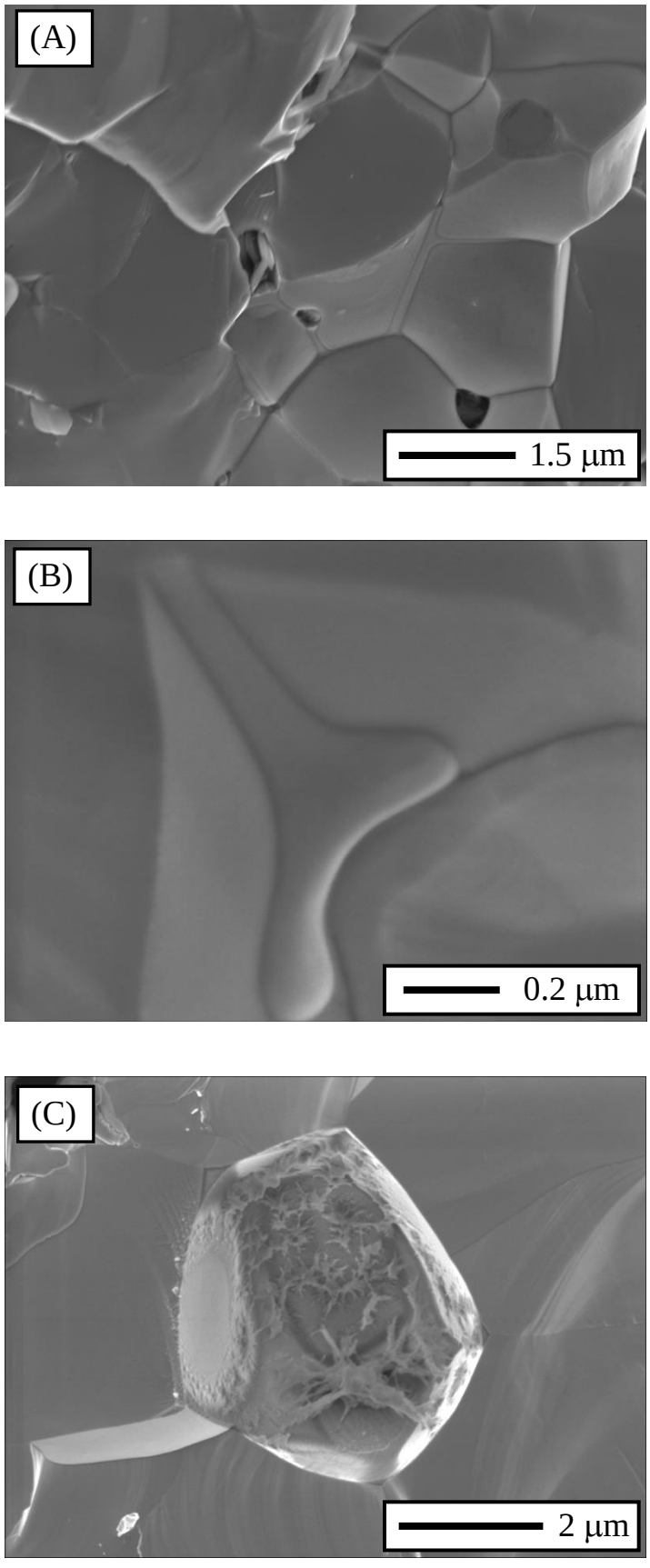

V. Zamora *et al.*
Figure 5

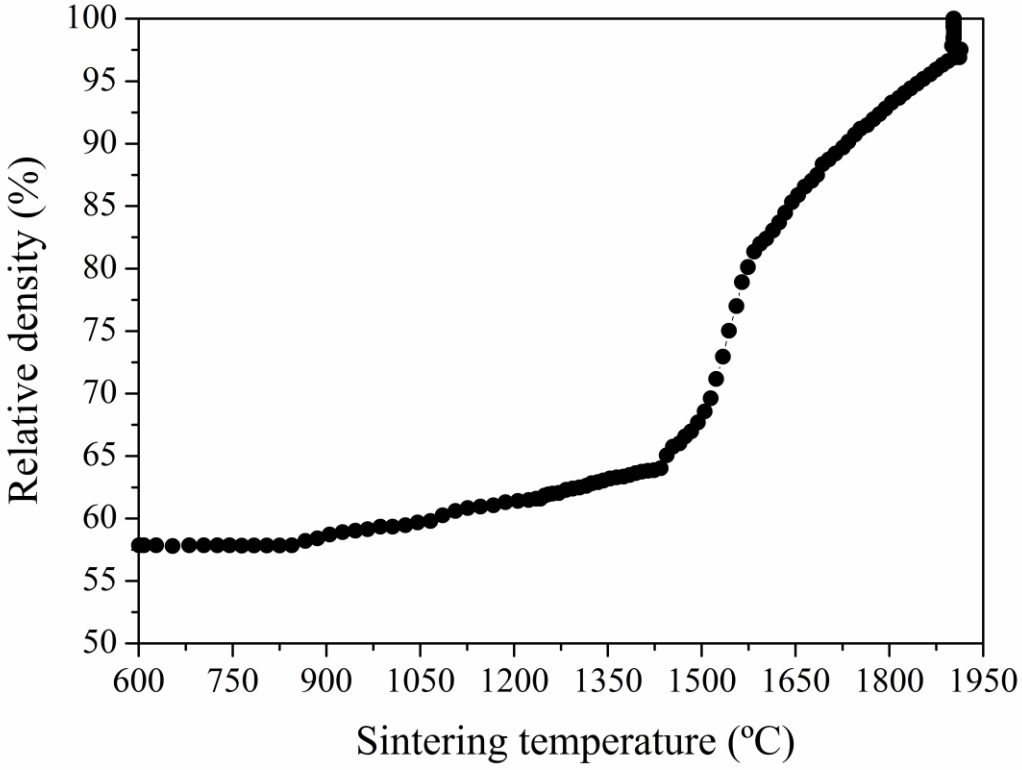

V. Zamora *et al.*
Figure 6

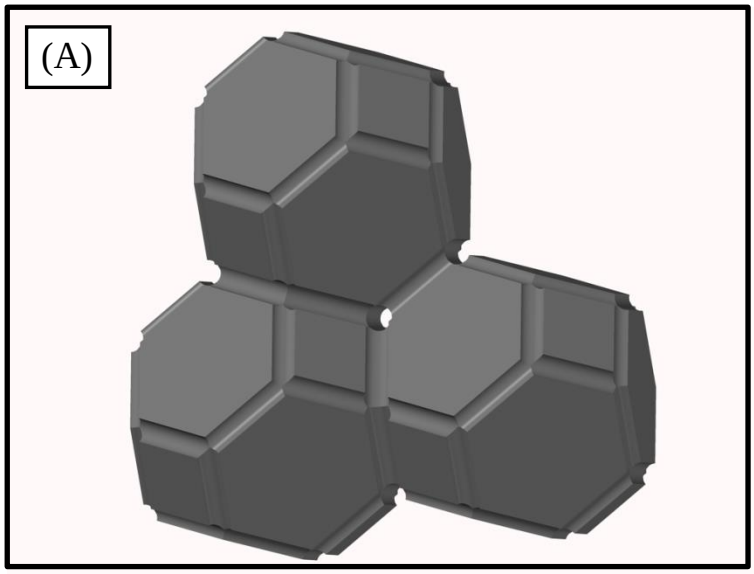

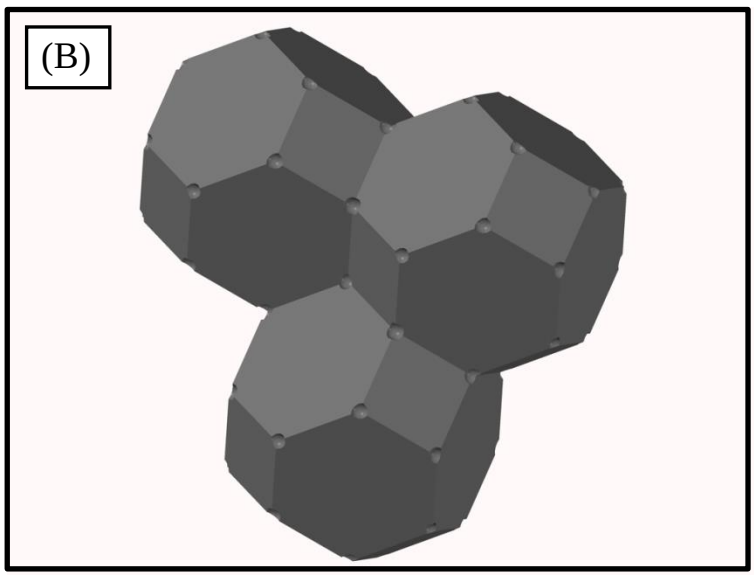

V. Zamora *et al.*
Figure 7

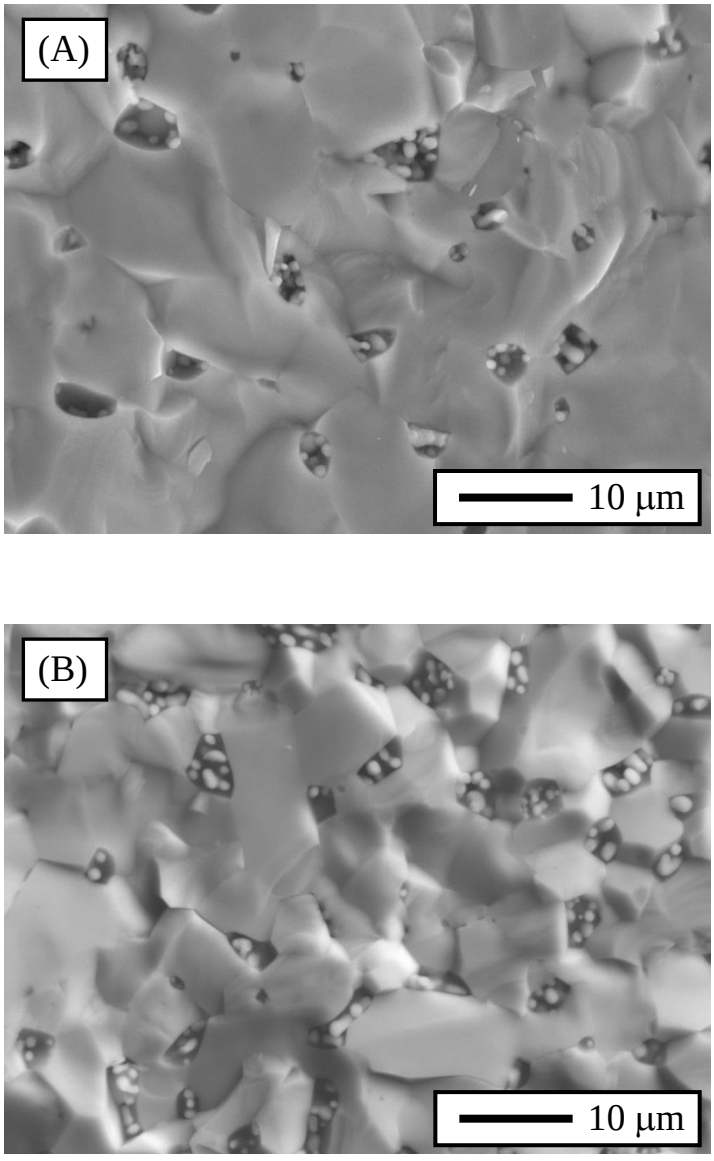

V. Zamora *et al.*
Figure 8